

Article

Influence of Rotor Inflow, Tip Loss, and Aerodynamics Modeling on the Maximum Thrust Computation in Hover

Berend G. van der Wall 

German Aerospace Center (DLR), Institute of Flight Systems, 38108 Braunschweig, Germany;
berend.vanderwall@dlr.de

Abstract: Comprehensive rotorcraft simulation codes are the workhorses for designing and simulating helicopters and their rotors under steady and unsteady operating conditions. These codes are also used to predict helicopters' limits as they approach rotor stall conditions. This paper focuses on the prediction of maximum rotor thrust when hovering (due to stall limits) and the thrust and power characteristics when the collective control angle is further increased. The aerodynamic factors that may significantly affect the results are as follows: steady vs. unsteady aerodynamics, steady vs. dynamic stall, blade tip losses, curvature flow, yaw angle, inflow model, and blade-vortex interaction. The inflow model and tip losses are found to be the most important factors. For real-world applications vortex-based inflow models are considered the best choice, as they reflect the blade circulation distribution within the inflow distribution. Because the focus is on the impact of aerodynamic modeling on rotor stall, the blade design and its flexibility are intentionally not considered.

Keywords: rotorcraft; aerodynamics; rotor stall; rotor blade tip loss; rotor inflow; prescribed wake; free-wake



Citation: van der Wall, B.G. Influence of Rotor Inflow, Tip Loss, and Aerodynamics Modeling on the Maximum Thrust Computation in Hover. *Aerospace* **2024**, *11*, 357. <https://doi.org/10.3390/aerospace11050357>

Academic Editors: Bo Cheng, Umberto Saetti and Pierluigi Capone

Received: 20 February 2024

Revised: 25 April 2024

Accepted: 27 April 2024

Published: 29 April 2024



Copyright: © 2024 by the author. Licensee MDPI, Basel, Switzerland. This article is an open access article distributed under the terms and conditions of the Creative Commons Attribution (CC BY) license (<https://creativecommons.org/licenses/by/4.0/>).

1. Introduction

Since the end of the 1920s, when autogyros emerged as the first rotating-wing aircraft, and 10 years later with helicopters, the trimmed maximum thrust capability of their main rotor has been of interest. It defines the aerodynamic limit of the operational envelope from hover (helicopters only) or minimum speed (autogyros) to their maximum speed and maximum ceiling height. In those times, the blade rotational speed of both types of rotating-wing aircraft was rather low with a blade tip Mach number of around 0.4. Therefore, the envelope of rotor operation was essentially limited by the stall and reversed flow conditions on the blades, and not yet by compressibility effects on the advancing side.

Bailey, Gustafson and Myers at NACA experimentally investigated rotor blade stall on a YG-1B autogyro via observation of tufts attached to the blade surface [1,2]. In Germany, Sissingh extended rotor aerodynamic theory to include steady airfoil stall, yawed flow effect on airfoil characteristics, and compressibility effects [3]. In helicopter developments at the Focke and Flettner companies, compressibility effects were known to become important for future high-speed rotorcraft, as highlighted by Focke [4]. German knowledge on rotorcraft theory and experiments was summarized after the Second World War [5].

By the end of the 1960s, the rotor blade tip Mach number of helicopters increased to values of around 0.65, balancing retreating blade stall and advancing blade compressibility effects for optimum helicopter performance throughout the flight regime. The centrifugal forces and the dynamic pressure (and with it the rotor thrust capability) acting on the rotor blades therefore rose twofold, with the power required being threefold.

In the early 1970s, the rotor limits were explored numerically and experimentally, mainly at high speed and with a focus on retreating blade stall. Bellinger [6] found by comparing theory with full-scale measurements of a H-34 rotor, that modeling unsteady

airfoil characteristics significantly improves the rotor lift prediction, albeit not fully sufficiently. Variable inflow and blade flexibility in flap and lag appeared unimportant, but elastic torsion was found to play a primary role, as it directly affected the angle of attack.

The effect of the Reynolds number on rotor stall was investigated by Hardy [7] on 2D data for the Vertol 23010-1.58 airfoil. A large influence on the maximum lift coefficient was found at low Mach numbers. Up to Mach numbers of 0.6, this effect diminished. For an advance ratio of 0.3, rotor measurements were made with fixed collective and zero cyclic control angles. The shaft angle varied from -35 deg to zero with a progressive stall development and associated reduction in the rotor lift curve slope.

McCroskey [8] performed 1:7.5 model-scale CH-47C rotor experiments with a pressure sensor instrumented blade section at 75% radius. In hover measurements, the rotating blade stall was still showing the leading-edge pressure peak, while in the 2D data, the peak collapsed, resulting in higher maximum lift coefficients in the rotating case. In forward flight with an advance ratio of $\mu = 0.35$, rotor stall was investigated with a fixed collective control angle by varying the shaft angle of attack as was implemented by Hardy [7]. No trim was performed on the rotor and only stall characteristics were studied.

Landgrebe and Bellinger [9] performed an experimental study on model rotor stall with eight variations of twist, airfoil, taper, number of blades, and torsional frequency, while keeping radius, chord, tip Mach number, and hinge offset constant. Because of a very low tip Mach number below 0.3, only minor compressibility effects were observed. Again, no cyclic control angle was used to trim the rotor.

Amer and LaForge [10] showed that the maximum steady thrust capability of teetering and articulated rotors is the same in the range of advance ratios from $\mu = 0.25$ to 0.36, based on trimmed flight test data at the never-exceed velocity for different flight levels. The maximum thrust was also found to be the same during unsteady pull-up maneuvers at advance ratios ranging from $\mu = 0.15$ to 0.39.

McHugh [11] examined the lift limits of a 1:10 model-scale CH-47B/C rotor by using wind tunnel tests from hover up to advance ratios of $\mu = 0.64$. The rotor was trimmed to lift, propulsive force, and minimum flapping by the rotor control angles and the shaft angle. He found the maximum trimmed rotor lift limits to depend on the propulsive force $C_D/(\Lambda\sigma)$ applied; see Figure 1. $\Lambda = 4/\pi$ is the rotor disk aspect ratio, and C_D is the helicopter drag coefficient.

Much later, Yeo [12] used CAMRAD II [13] to calculate the rotor performance and loads of McHugh's experiments. His results for model-scale Reynolds numbers (Re_{ms}) are shown below the model-scale test data; see Figure 1. Computations with full-scale Reynolds numbers (Re_{fs}) with higher maximum lift coefficients of the same airfoil are depicted above the model-scale data.

In addition, Johnson [14] sketched the lift limits of modern rotors (with advanced airfoils and modern blade planforms) in level flight from hover to high advance ratios; see Figure 1. With increasing advance ratio, the maximum rotor lift capability reduces due to the increasing asymmetry of dynamic pressure on the advancing and retreating sides. This limits the capability of trimming the rotor, especially due to stall on the retreating side.

The availability of computers enabled engineers to develop comprehensive simulation codes (e.g., CAMRAD II [13]) for a fast evaluation of helicopter and rotor performance, including dynamics, aerodynamics, and the rotor wake with an ever-increasing variety of models and refinements, representing the physics in an engineering manner.

In pre-design studies and real-time helicopter simulations, the simplicity of these models is essential, yet these must simultaneously represent the main features reliably well and physically correctly. Look-up tables are often used for aerodynamic coefficients and are set up for the required range of Mach numbers and angles of attack. They include steady stall characteristics and the compressibility of the airfoils used, but are lacking unsteady aerodynamics such as dynamic stall with stall delay and post-stall vortex shedding. Yawed flow is present everywhere in forward flight and causes an advantageous stall delay. Centrifugal forces in the boundary layer, especially at the inboard regions of a rotating

blade with large curvature flow, also delay stall. These effects are usually not covered by look-up tables, because they would require multi-dimensional tables.

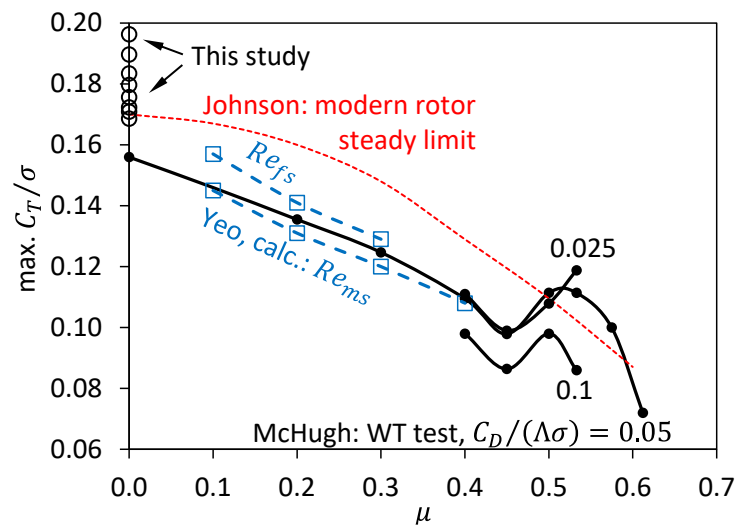


Figure 1. McHugh’s maximum rotor lift limits curve, 1 : 10 scale CH-47B/C rotor, 620 ft/s tip speed, with Yeo’s calculations [12] of model- and full-scale Reynolds numbers and Johnson’s level flight limits of modern rotors [14].

For the prediction of the maximum rotor lifting capabilities, the ability to model dynamic stall in combined unsteady yaw and periodic free-stream velocity becomes increasingly important, as demonstrated in a GARTEUR activity about dynamic stall and blade torsion [15]. Measurements on a model rotor with reduced tip speed at an advance ratio of $\mu = 0.4$ were used to validate and improve comprehensive codes. The rotor was trimmed as in the wind tunnel to a prescribed shaft angle, rotor lift, and propulsive and lateral forces. Deep stall was encountered on the retreating side with increasing rotor lift. The simulations using comprehensive rotor codes were only able to trim to the highest measured rotor lift (if at all), when both dynamic stall and yawed flow models were enabled.

The AIAA Rotorcraft Hover Prediction Workshop [16] provides data from three model-scale rotors up to a blade loading of $C_T/\sigma = 0.1$ for a UH-60A rotor measured in 1983, and 0.125 for the HVAB rotor tested in 2022 [17], but without reaching or exceeding the stall limits. Recently, the measurements of a rotor in axial flow up to and beyond rotor stall provide some experimental data in these regimes, although not really in hover, but rather under an aerodynamic climb condition [18], supporting the interest in the topic of maximum rotor thrust. The prediction activities of the workshop essentially make use of computational fluid dynamics codes (see the publications of [16]). A variety of advanced comprehensive codes, beginning with the lifting surface method for blade aerodynamics, that were coupled to advanced curved vortex element free-wake code, and higher-level wake methods up to the vorticity transport model (VTM), were presented in [19], with a revision given in [20]. Despite the higher level, the VTM predicted a premature deep stall, compared to the experiment of [16], while the free-wake method did not.

In comprehensive rotor codes, the blade pitch angle (control angles, pretwist, and elastic torsion distribution) and the induced inflow model used are essential for the computation of the local aerodynamic angle of attack, and thus the prediction of stall onset at large thrust. A variety of induced inflow models exist that are based on momentum theory (constant inflow or with longitudinal and/or lateral inflow gradients), potential theory, and vortex theory (with prescribed or free-wake geometry). The loss of lift due to flow around the blade tip is often treated by simply cutting off the two-dimensional lift distribution at an “effective” non-dimensional radial station B (its equivalent at the blade root is usually neglected). This simultaneously increases the mean induced inflow ratio

because of the reduced effective rotor disk area. Such a crude approximation does not represent the actual cause of the lift dropping to zero at the end of the blade, i.e., the induced velocities due to the airflow around the blade tip. Therefore, a more physical approach should be used, such as the Prandtl/Betz formulation [21], or a simpler approximation of it. Since all these models impact the capability of comprehensive codes to predict the trimmable rotor thrust limits in hover and forward flight, their impact and importance are investigated in this paper. The rotor blade is treated as stiff in this study in order to isolate the influences of aerodynamic modeling from the blade design parameters (e.g., geometry, taper, twist, sweep, an-/dihedral, elasticity, airfoil selection). A Mach-scaled Bo105 model rotor geometry is taken as a basis here.

Other limits, most often reached before the aerodynamic rotor limits, such as structural load limits, maximum available power, and mechanical limits of blade pitch control, are ignored in this study to focus on the pure aerodynamic limits that represent the boundary of a trimmable rotor with maximum possible thrust.

This article demonstrates the capabilities of combining low-level, semi-empirical methods for blade section aerodynamics, tip loss, curvature flow stall delay, and a variety of inflow models, with respect to the maximum rotor lift computation. Such modeling has the advantage of very low computational effort (a necessity in the early design stage), and the impact of each individual model on the results will be shown. The article is based on a conference paper of the author [22], expanded by the inclusion of yet unpublished free-wake computation results. The range of results for maximum trimmable thrust obtained in this study is indicated by the circles under the hovering condition ($\mu = 0$) in Figure 1.

2. Semi-Empirical Physical Models

2.1. Rotor Blade Model

A Mach-scaled Bo105 model rotor with rectangular blades is used here, and its characteristics are given in Table 1. Rotor radius and root cutout are scaled to 40.73% of the full-scale vehicle, while the chord length is scaled to 44.81% to partially account for loss of maximum lift capability due to the lower Reynolds numbers of the model rotor. Thus, the resulting solidity σ is 10% greater than that of the full-scale rotor, while the tip Mach number is the same. The nominal thrust coefficient is based on a 2.46-ton Bo105 as a starting value for a thrust sweep towards the maximum trimmable limit.

Table 1. Mach-scale model rotor characteristics.

Characteristic	Symbol	Metric
Rotor blade radius	R	2.0 m
Rotor blade chord length	c	0.121 m
Aerodynamic root cutout	y_a	0.44 m
Radius of zero twist angle	y_{tw}	1.5 m
Number of rotor blades	N_b	4
Rotor blade precone angle	β_p	2.5 deg
Blade pretwist per radius	Θ_{tw}	−8 deg
Airfoil, tabbed trailing edge	NACA	23012
Rotor speed of rotation	Ω	109 rad/s
Rotor blade tip speed	ΩR	218 m/s
Hover tip Mach number	M_h	0.639
Rotor solidity	σ	0.077
Nominal thrust coefficient	C_T	0.00547
Nominal rotor blade loading	C_T/σ	0.071

DLR's high-resolution rotor simulation code S4 is used; a detailed description of its features is given in [23]. The rotor blade is represented by 20 elements of equal annulus area in the rotor disk, leading to wider elements at the root (where low dynamic pressure is present) and progressively smaller ones towards the blade tip (with the highest dynamic pressure and where the largest radial gradients of lift are to be expected); see Figure 2.

The dashed line marks the pitch axis at quarter-chord and the + symbols denote the aerodynamic collocation points at three-quarter chord. The velocities acting normally and tangentially to the chord line are computed there, including the pitch rate (due to blade pitch control) times semi-chord. However, in hover, the blade pitch angle is constant and therefore the pitch rate remains zero.

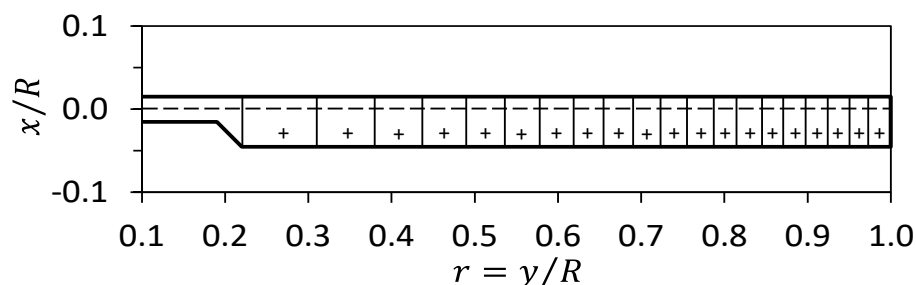


Figure 2. Model rotor, 20 blade element distribution.

2.2. Airfoil Model

The classical way to compute section lift, drag, and the moment coefficient in comprehensive codes is based on a steady look-up table. With the local Mach number and angle of attack, both computed by the velocity components acting on the section of interest, the aerodynamic coefficients are interpolated from the table. Although compressibility and steady stall effects are included, yaw and curvature flow effects and dynamic stall are missing, because these would require multi-dimensional tables. The impact of all of these on the delay of the steady stall angle of attack α_{ss} —and hence the capability of the representation of dynamic stall hysteresis including lift overshoot—calls for a semi-empirical, physics-based analytical formulation of the airfoil coefficients instead of using look-up tables.

Starting in the 1970s, several unsteady aerodynamic methods—partly based on the tables with the addition of unsteady contributions and partly fully analytical computations of the coefficients—have been developed, e.g., by Gormont [24], Bielawa [25], Tran [26], Beddoes [27], Gangwani [28], Leiss [29,30], Leishman [31], Petot [32], and Truong [33].

Here, the Leiss model [29,30], applied to the NACA 23012 airfoil [34] (as used on the Bo105 rotor blades), is used. Its advantage is the fully analytical mathematical formulation without any if-then-else decisions, resulting in smooth lift, drag, and moment curves under steady and unsteady conditions. The model parameters are identified using airfoil data obtained in the wind tunnel or via CFD for the range of Mach (and associated Reynolds) numbers and angles of attack exceeding the stall in positive and negative directions (for both flow from the front and back). The analytical formulation ensures physical results even far beyond the regimes covered in the database, and also inherently includes reversed flow.

The Leiss model has been applied to other airfoils and was validated, e.g., in [15]. The airfoil coefficients of this model act at the quarter-chord point normal to the chord line ($C_Z = C_n M^2$, positive up) and in a chordwise direction ($C_X = -C_c M^2$, positive forward), while the moment acts about the quarter-chord point ($C_M = C_m M^2$, positive nose-up). These aerodynamic coefficients are based on the sonic speed dynamic pressure, and hence, they directly represent non-dimensional forces and moments. In traditional comprehensive rotor codes, the local dynamic pressure is used, such that the coefficients represent the local aerodynamic characteristics, but not the radial distribution of forces and moments. The conversion of these coefficients from the aerodynamic coordinate system to the airfoil coordinate system is shown in Figure 3.

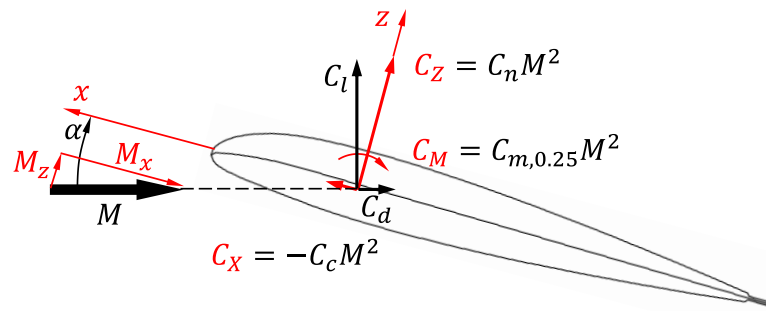


Figure 3. Conversion of aerodynamic coefficients.

The fully analytical, semi-empirical formulation includes compressibility effects and stall, and covers the entire range of angles of attack from $\alpha = -180$ deg to $+180$ deg in purely analytical form. Reversed flow, however, usually is confined to Mach numbers of $M_h(r_a - \mu)$ at $\psi = 270$ deg azimuth on the retreating side (M_h is the blade tip Mach number in hover and r_a is the non-dimensional blade root cutout), which for this rotor reaches a maximum value of $M = -0.179$ (indicating reversed flow) for a high advance ratio of $\mu = 0.5$. In this case, the advancing tip at $\psi = 90$ deg azimuth already experiences a Mach number of $M_h(1 + \mu) = 0.959$.

The steady stall angle of attack α_{ss} depends on the Mach number M and is large in incompressible flow, while in the higher subsonic speed range it progressively approaches much smaller values. At nominal rotational speed of the rotor, the variation of α_{ss} is given in Figure 4. The circles denote the radial distribution of blade element aerodynamic collocation points. The Mach number here also is a direct measure of the blade radial coordinate r , as they are proportional to one another: $M = M_h r$.

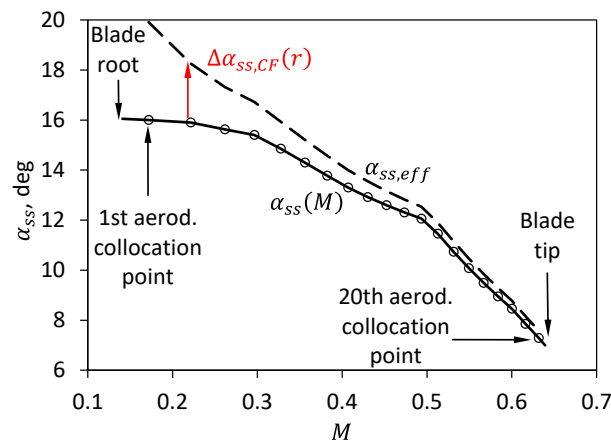


Figure 4. Steady stall angle of attack in hover, without (solid) and with inclusion of curvature flow (CF) effect (dashed).

Rotating wing experiments both in hover and with axial flow revealed that—especially inboard near the hub—the curvature flow (CF) acting on the boundary layer generates significantly higher maximum lift coefficients, compared to 2D flow conditions. This effect progressively dies out towards the blade tip and can be interpreted as a shift of the steady stall angle of attack to higher values. Viterna and Corrigan [35] suggested a global correction of airfoil lift and drag coefficients in the context of wind turbine simulations. Airfoil tables in comprehensive rotor codes often empirically extend the attached flow regime of lift, drag, and moment coefficients by some degrees in the range of Mach numbers up to ca. 0.4, i.e., mainly in the inner portion of the rotor blade. In this study, that effect is simulated empirically by an offset $\Delta\alpha_{ss,CF}(r) \propto 1/r$ with the value at the blade root r_a as the sole characteristic parameter. In this study, an empirical value of $\Delta\alpha_{ss,CF}(r_a) = 4$ deg is used. For large radii, this stall offset approaches zero and then represents the 2D airfoil

characteristics. It is understood that this is a crude approximation and requires reliable data for a better representation of the physics, but it is at least a physically reasonable approach for studying the impact of such an effect on rotor stall. In application, this offset is used the same way as if it was caused by a yaw angle, also delaying the stall angle of attack.

The conversion of the Leiss's coefficients to the classical lift, drag, and moment coefficients based on the dynamic pressure of the velocity components is shown in Figure 3 and given by Equation (1). The trigonometric functions can be replaced by the Mach components acting in the chordwise direction, M_x , and normal to it, M_z : $\cos \alpha = M_x/M$ and $\sin \alpha = M_z/M$:

$$\begin{aligned} C_l &= (C_Z \cos \alpha + C_X \sin \alpha) / M^2 = (C_Z M_x + C_X M_z) / M^3 \\ C_d &= (C_Z \sin \alpha - C_X \cos \alpha) / M^2 = (C_Z M_z - C_X M_x) / M^3 \\ C_m &= C_M / M^2 \end{aligned} \quad (1)$$

Two examples for lift, drag, and moment coefficients are given in Figure 5, where the black line represents the 2D steady airfoil characteristics without the CF effect, and the red line with the inclusion of it, for two radial stations (Figure 5a inboard and Figure 5b outboard), and their respective Mach numbers. Figure 5a shows the data for the first blade element with $r = 0.269$, $M = 0.172$, i.e., incompressible flow, and Figure 5b shows the data for $r = 0.964$, $M = 0.618$ in the compressible range near the blade tip.

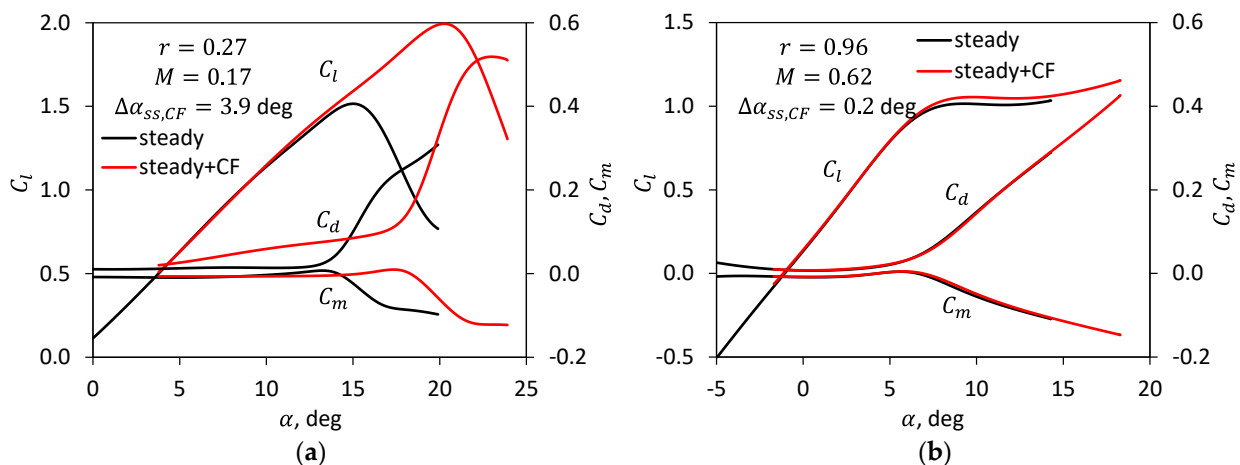


Figure 5. Steady airfoil characteristics in hover, without (black lines) and with inclusion of curvature flow (CF) effect (red lines). (a) incompressible flow regime near the blade root; (b) compressible flow regime near the blade tip.

The example is computed with the rotor at nominal speed of rotation in hover without inflow or tip loss, with steady aerodynamics, both without and with the CF model. The range of angles of attack is obtained by a collective control angle at 75% radius of 6 deg (without CF) and 10 deg (with CF) to include the stall angle in both cases. A 10 deg cyclic control angle is applied to cover a sufficient range of angles of attack.

Real-world steady post-stall conditions result in unsteady aerodynamic coefficients with stochastic variations of frequency and magnitude, due to permanent vortex shedding. Although a model for such post-stall vortex shedding (VS) with some randomness in shedding frequency and magnitude of fluctuations was developed in the 1990s [15], a reduced form is used here. It includes a fixed frequency (depending on the Mach number) and a constant magnitude in deep stall, which diminishes when approaching the stall angle of attack. This is shown exemplarily in Figure 6 for a non-dimensional radial station of $r = 0.598$ ($M = 0.38$). The computational setup is as before, without the CF effect, but with a collective control angle of 10 deg and 15 deg cyclic control applied to cover a range far enough above the stall angle. The thick black line represents the airfoil data without the VS model; the thin line represents the airfoil data with it.

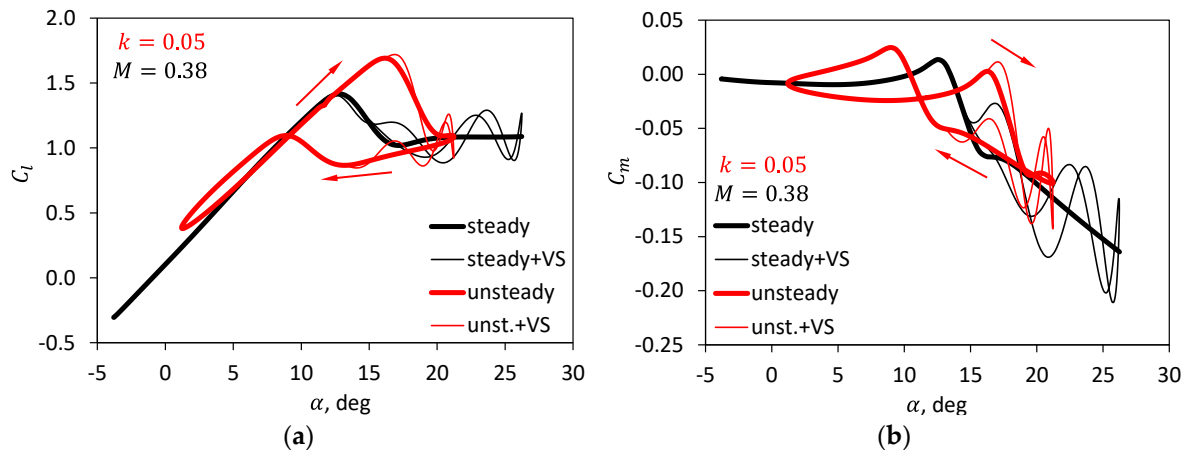


Figure 6. Steady (thick black lines) and unsteady (thick red lines) airfoil characteristics in hover, without and with inclusion of vortex shedding (VS) effect (thin lines). (a) lift coefficient; (b) moment coefficient.

Because this application with a cyclic control angle is an unsteady motion, the unsteady aerodynamics model needs to be switched on, which adds three effects: first, a phase delay of the effective angle of attack relative to the geometric incidence angle as described by the Theodorsen function [36]; second, a stall onset delay and that of flow reattachment; third, apparent masses (non-circulatory forces and moments).

The phase delay results in a hysteresis; the stall delay causes a significant lift overshoot in the upstroke motion, and a significant delay in flow reattachment during the downstroke. All this is shown by the red curves in Figure 6, where the mean angle is the same as for the steady data, but the amplitude of the cyclic control angle is reduced to 10 deg. In addition, the thin red line indicates the additional dynamics from when the VS model is switched on.

A validation of the model with experimental steady and unsteady data of an OA213 airfoil in 2D flow (yaw angle $\beta = 0$ deg) and under the $\beta = 22$ deg yawed flow condition at a Mach number of 0.18 was performed within a GARTEUR activity [15]. Steady measurements were performed first with time-averaged results; thus, no vortex shedding in the stalled region could be seen. The airfoil was periodically pitched at a reduced frequency of $k = (\omega c)/(2V) = 0.05$, and data for several individual successive cycles were made available. The VS model included random variations of frequency and magnitude in the GARTEUR study, such that each cycle is different, as in the experiment. Lift and moment coefficients are compared to the model in Figure 7.

The model correctly predicts both the steady and unsteady lift coefficient loops, as well as the difference between unyawed (Figure 7a) and yawed conditions (Figure 7b). The latter exhibits a smaller lift curve slope, a thinner dynamic stall hysteresis, and a slightly higher maximum lift coefficient at a significantly higher stall angle of attack, both in the steady and unsteady cases.

The aerodynamic moments shown in Figure 7c for the unyawed case and in Figure 7d for the yawed condition also reveal that the model correctly predicts the change of the steady and dynamic airfoil characteristics. As in the case of the lift coefficient, the yaw angle shifts the moment stall (steady and unsteady) to larger angles of attack. Drag data were not available; thus, they cannot be compared here with the experimental data.

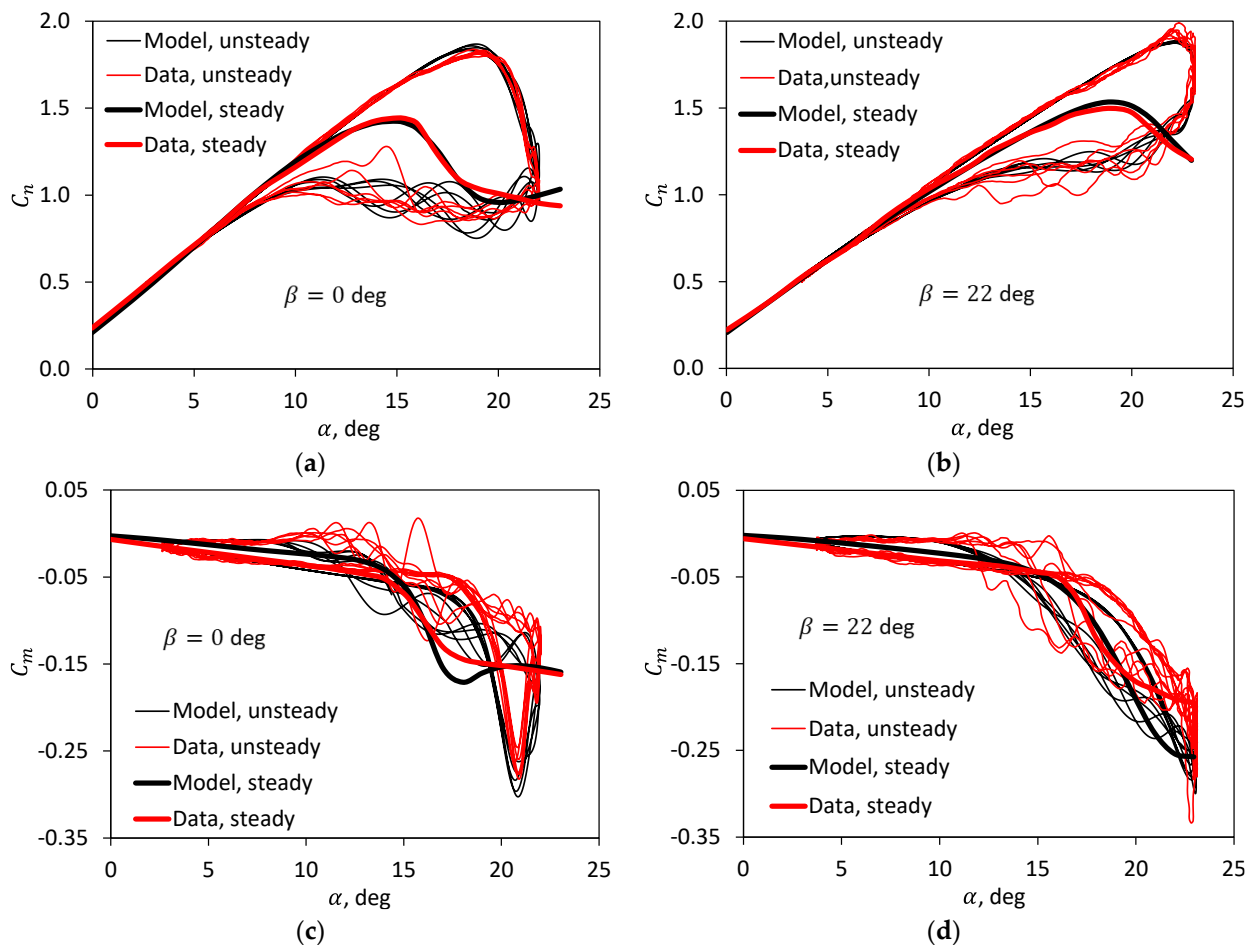


Figure 7. Steady (black) and unsteady (red) airfoil characteristics in hover, without and with inclusion of vortex shedding (VS) effect. (a) normal force coefficient, unyawed; (b) normal force coefficient, yawed; (c) moment coefficient, unyawed; (d) moment coefficient, yawed.

2.3. Rotor-Induced Inflow Models

The inflow models investigated were as follows: constant inflow (the “Glauert” model) from momentum theory [37], inflow including linear longitudinal and lateral variation (the “Drees” model) [38], a potential theory-based model with nonlinear radial and multi-harmonic circumferential distribution (the “Mangler” model) [39], a vortex wake method with computationally efficient prescribed geometry (called prescribed wake, “PW”) as used by DLR, e.g., in [23], and a free-wake model developed at DLR [40].

In hover, Glauert and Drees are identical, just the Mangler model has a nonlinear radial variation of induced velocities, but is constant in circumference. In forward flight, the Drees model has a longitudinal and lateral gradient relative to the constant mean values of Glauert’s model. The Mangler model is laterally symmetric, which leads to a non-linear longitudinal gradient, and results in radially nonlinear distributions with multi-harmonic periodic variation in the circumference of the rotor disk.

The prescribed wake (PW) model generates nonlinear inflow distributions all over the disk. It is fed by trailed vorticity all along the span within the near wake. Up to three trailed vortices are kept in the far wake: one at the root, one at the tip, and—depending on the lift distribution near the tip—a secondary more inboard tip vortex of an opposite sense of rotation.

The wake contraction and its convection are prescribed, and its geometry was originally based on Beddoes’ model [41], and was later on significantly enhanced to include both the root cutout region and harmonic loading effects on the wake geometry perturbations [42], as well as the perturbations due to the presence of a fuselage [43].

DLR's in-house development of a free-wake (FW) code originated from the mid-1990s for code enhancements related to higher harmonic rotor blade control for vibration and noise reduction purposes [40]. The free-wake consists of five revolutions behind the blades, which is sufficient for the high thrust levels investigated here. Eleven trailers are fitted to the blade elements, and the azimuthal resolution is 10 deg segments, but time integration of the geometry is performed with 2 deg azimuth steps.

An example of the free-wake structure obtained in hover at high thrust is shown in Figure 8. It is cut across the center to show the radial variation of vertical convection of the vorticity sheets, following the radial induced inflow distribution. At the bottom, the wake truncation is visible with reduced wake convection due to the missing remainder of the wake to infinity.



Figure 8. Free-wake structure in hover, $C_T/\sigma = 0.16$. The colors represent the trailed vorticity strength. Red = tip vortex with high positive vorticity, blue = inboard vorticity with moderate to low negative values.

A weak coupling strategy between the rotor air loads computation, the free-wake geometry iteration, and its induced velocity computation at the blade elements was employed, and a trim to desired thrust (or power) was performed with the collective control angle. In hover, the aerodynamics of an isolated rotor are considered stationary, because a blade element experiences constant velocities and angles of attack throughout the revolution. Under these conditions, only trailed vorticity is fed into the wake, based on radial gradients of the blade bound circulation distribution. Usually, after four to five iterations, the rotor aerodynamics, the wake geometry, and the wake-induced velocities acting at the rotor blades are converged. A trim to thrust near its maximum value is difficult because the gradient $dT/d\Theta$ approaches zero. Beyond the maximum thrust, that derivative initially reverses its sign until the thrust curve flattens out and gradually rises again, similar to the steady lift curves shown in Figures 5–7. A trim to thrust therefore is difficult and requires a proper initial value of the collective control angle to converge.

In this region, a trim to rotor power converges quickly, because the gradient $dP/d\Theta$ progressively increases with thrust throughout the rotor stall regime. The drawback of trim

to power is that some iterations are needed in order to compare the results for the same thrust under these post-stall conditions. Alternatively, a stepwise increase in the collective control angle without trim and just converging the result will also produce the thrust curve, and the finer steps around the maximum thrust can be used to identify the maximum itself. Again, the drawback of this procedure is that some iterations are needed to obtain the same thrust with the various models employed for a direct comparison.

Hovering is a difficult condition for a free-wake solution due to the inherent wake instability and roll-up caused by wake truncation at the end of the computed wake. To avoid these instabilities and to obtain a quasi-steady solution, the contraction and convection are considered final after a specified wake age (e.g., one or two revolutions behind the blade). For the remaining wake, the radial displacements of vortex filaments are suppressed. The reasoning for this is to simulate an ideal infinitely long wake. Although wake elements far away from the rotor practically do not contribute to induced velocities at the rotor, they influence the truncated end of the limited wake length used in simulations. The suppression of radial displacements results in an almost cylindrical wake (quite comparable to a prescribed wake) without instabilities. It still results in a reduced convection speed at the truncated end, which results in a closer proximity of the wake sheets than in the region above. At low thrust, where the wake remains close to the rotor, this would overpredict induced velocities at the rotor. However, for the high thrust conditions investigated here, the wake end is sufficiently far away from the rotor.

An example radial distribution of induced inflow ratio in hover for all these models is shown in Figure 9. The Mangler model represents a distribution similar to an expected lift distribution. The PW distribution is more parallel to the constant inflow up to 80% radius, and near the tip, the inflow decreases due to the wake contraction and the upwash generated by the tip vortices of the preceding blades. The FW inflow distribution is close to the PW for the blade tip region, and inboard of 80% radius around the middle between the Mangler and PW models. The mean value, however, is the same for all models.

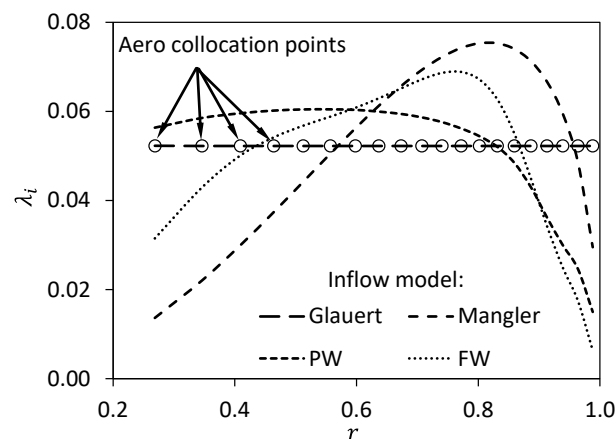


Figure 9. Example distributions of induced inflow ratio from various models in hover, $C_T/\sigma = 0.071$.

2.4. Tip Loss Model

The simple but non-physical cutting off of the blade tip at a non-dimensional effective radius B is often used in comprehensive codes (mostly selected as $B = 0.97$). Alternatively, it can be computed based on the thrust coefficient as $B = 1 - \sqrt{2C_T}/N_b$, a simplified result derived by Prandtl [21]. Wheatley [44] suggested a tip loss factor independent of thrust, based on the blade chord-to-radius ratio: $B = 1 - c/(2R)$, and similarly, Sissingh [3,45] by $B = 1 - c/(1.5R)$. The blade element aerodynamics are treated as purely 2D from the blade root to the effective radius B , and the momentum-based induced velocity is corrected due to the reduced rotor disk area by $\lambda_{i,eff} = \lambda_i/B$. Example values for B using the different methods are given in Table 2. At zero thrust, Prandtl's method results in 2D aerodynamics up to the blade tip, $B = 1$. With increasing thrust, it leads to smaller B , which appears more

physical due to the increased tip vortex strength and increased radial portions affected by it. For nominal thrust and twice this, the values computed by the other methods are rather close to Prandtl’s result.

Table 2. Examples for effective radius B , rotor data from Table 1.

C_T	C_T/σ	Prandtl [21]	Wheatley [44]	Sissingh [45]
0.00000	0.000	1.000	0.97	0.96
0.00547	0.071	0.974	0.97	0.96
0.01094	0.142	0.962	0.97	0.96
0.01641	0.213	0.954	0.97	0.96

In the S4 code, the tip losses are introduced in a semi-empirical manner by additional induced velocities, as if generated by a continuous trailed vorticity. The root losses are also accounted for in this manner. This allows the combination of any inflow model with more realistic lift losses in the tip and root regions. These additional induced velocities begin with zero at a radial station r_{tl} indicating the beginning of the tip loss region, and progressively increase until the zero-lift angle of attack is obtained at the blade tip itself. This leads to zero lift at the tip, as required, which approximates the Prandtl–Betz tip loss formulation [21]. The innermost element of the blade is treated the same way.

Various values for the tip loss parameter r_{tl} were investigated, namely 0.8, 0.9, 0.95, and 1.0 (which means no tip loss) to study its effect on the results. Considering a constant 2D lift coefficient of unity, the tip loss model leads to a continuous progressive drop towards zero in the tip and root regions, as shown in Figure 10a. The actual lift force distribution is based on the local dynamic pressure, i.e., proportional to $r^2 C_l$, and sketched in Figure 10b.

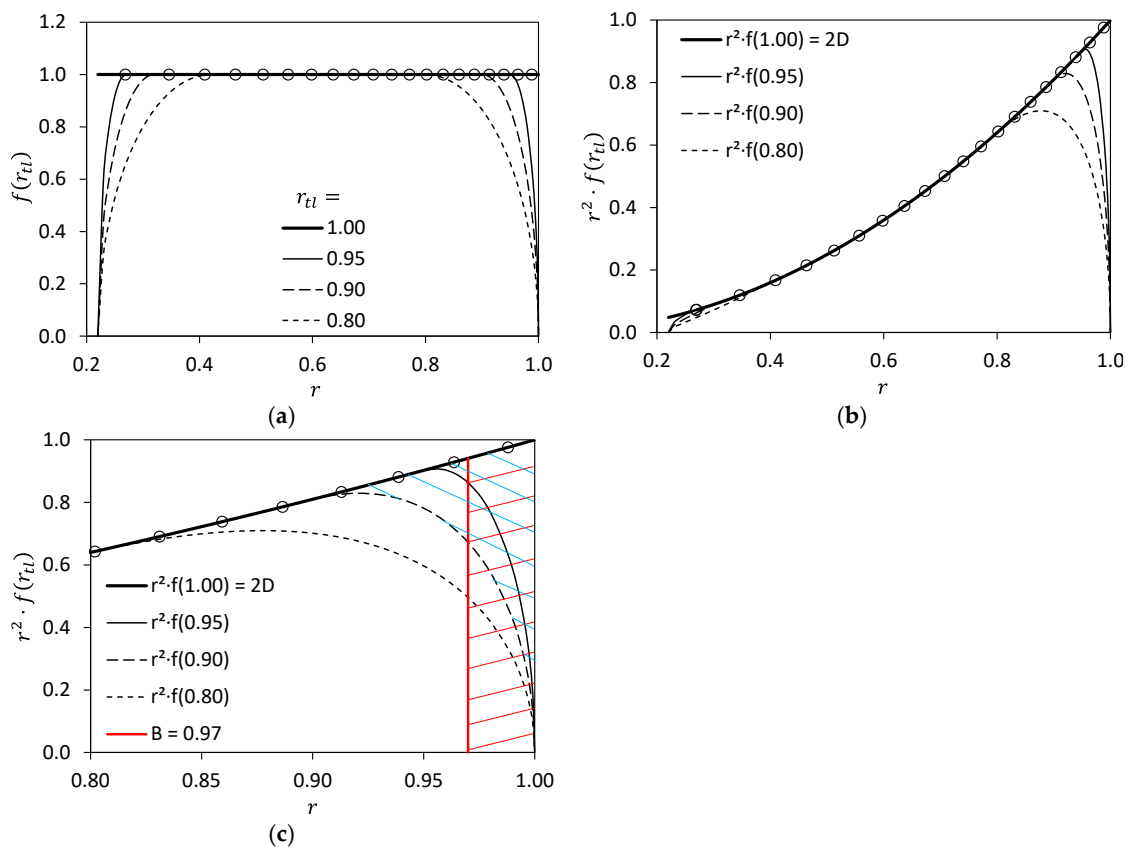


Figure 10. Root and tip loss impact on lift distribution for various r_{tl} values. (a) 2D lift coefficient of unity; (b) 2D non-dimensional lift, based on (a); (c) comparison of tip loss methods for various r_{tl} values from 0.8 to 1.

It appears justified to ignore the small overall loss at the root region, compared to that at the blade tip. It is interesting to note which value of r_{tl} approximately represents an equivalent to the loss caused by cutting off the blade at the typical value of $B = 0.97$. This is shown in Figure 10c, where only the tip region of Figure 10b is shown. The area hatched in red is the loss due to cutting off at B . It appears rather equivalent to selecting $r_{tl} = 0.9$, generating the loss of the area hatched in blue, which appears somewhat less than the red hatched area. $r_{tl} = 0.8$ will be more equivalent to a factor of $B = 0.96$.

3. Results and Discussion

3.1. General Remarks

In general, the following procedure is applied: a rotor trim is performed with a prescribed shaft angle and zero rotor hub rolling and pitching moments. It starts with a blade loading of nominal thrust ($C_T/\sigma = 0.071$) which is first increased in constant thrust increments. When stall onset is encountered, the increment is reduced to progressively finer steps until the maximum trimmable thrust is reached and the rotor lift curve slope with respect to the collective control angle becomes zero: $dC_T/d\Theta_{75} = 0$. This procedure is repeated for a range of parameter variations with the different aerodynamics models described in the previous section, for:

- Airfoil aerodynamics: steady/unsteady;
- CF model: off/on;
- VS model: off/on;
- Inflow model: Glauert/Mangler/PW/FW;
- Begin of tip loss: $r_{tl} = 0.8/0.9/0.95/1.0$.

The trim computation is based on a single blade only, assuming that all blades experience the same conditions at the same azimuth, which ensures the periodicity. The trim accuracy was set very tight to 1 N in thrust and 1 Nm in aerodynamic hub moments. For a maximum thrust in hover of up to 11 kN, this trim tolerance is less than 0.1 permille.

Due to a constant circumferential flow environment under the hovering condition, no cyclic control angles are needed for trimming the hub moments to zero, and hence $\Theta_C = \Theta_S = 0$ deg. The region above maximum rotor thrust ($C_{T,max}$) can also be explored by using $\Theta_{75} = \Theta_{75}(C_{T,max}) + 1, 3, 5$ and 10 deg of collective control angle settings. Such a further increase in the collective control angle reveals an initial loss of thrust due to increasing stall regions on the rotor blade. A further increase of Θ_{75} then again generates an increase in thrust, similar to the individual steady airfoil lift coefficient behavior when exceeding stall. In hover, the Glauert and Drees inflow models generate identical constant inflow all over the disk; hence identical results were obtained and only the Glauert model was applied here.

As long as the attached flow is present everywhere, a constant circumferential flow condition is a valid assumption. When stall occurs, unsteady flow structures develop, for example due to VS. In order to reduce the theoretical number of combinations of the above list, the VS and yaw models were individually applied only to the $r_{tl} = 0.9$ setting. The VS model introduces another difficulty, because the frequency of vortex shedding is modeled dependent on the Mach number, and therefore differs for each radial position. In general, it results in a non-integer harmonic of the rotor rotational frequency. Therefore, each individual revolution becomes slightly different and no steady mean rotor thrust nor hub moments can be obtained anymore. Then, sufficient thrust and hub moment thresholds must be specified when trimming the rotor, such that the thrust fluctuations remain within the thresholds specified.

In a real-world environment, this does not only affect the blade element(s) generating the VS, because the vortices also are released to the flow and will possibly be encountered by the following blades. However, VS will happen only at high thrust that comes along with a high induced velocity, transporting these disturbances downwards and away from the rotor. Therefore, here the assumption is made that such turbulence may be ignored and

each blade is operating in a generally undisturbed free-stream, even when experiencing deep stall with VS.

Consequently, the application of the unsteady aerodynamics model is no different from the steady model in this setup, but the VS model may be switched on to generate periodically oscillating aerodynamic coefficients of the blade elements operating in the post-stall regime. However, with or without the VS model, no difference in maximum C_T/σ was found in this study.

3.2. Rotor Thrust, Power, and Figure of Merit

The results for a thrust sweep from its nominal value to the individual maximum thrust ($C_{T,max}$) and up to $\Theta_{75}(C_{T,max}) + 10$ deg with every combination of the inflow model (Glauert, Mangler, PW, FW) are given in Figure 11. In addition, $r_{tl} = 0.9$ is also combined with the curvature flow model (CF).

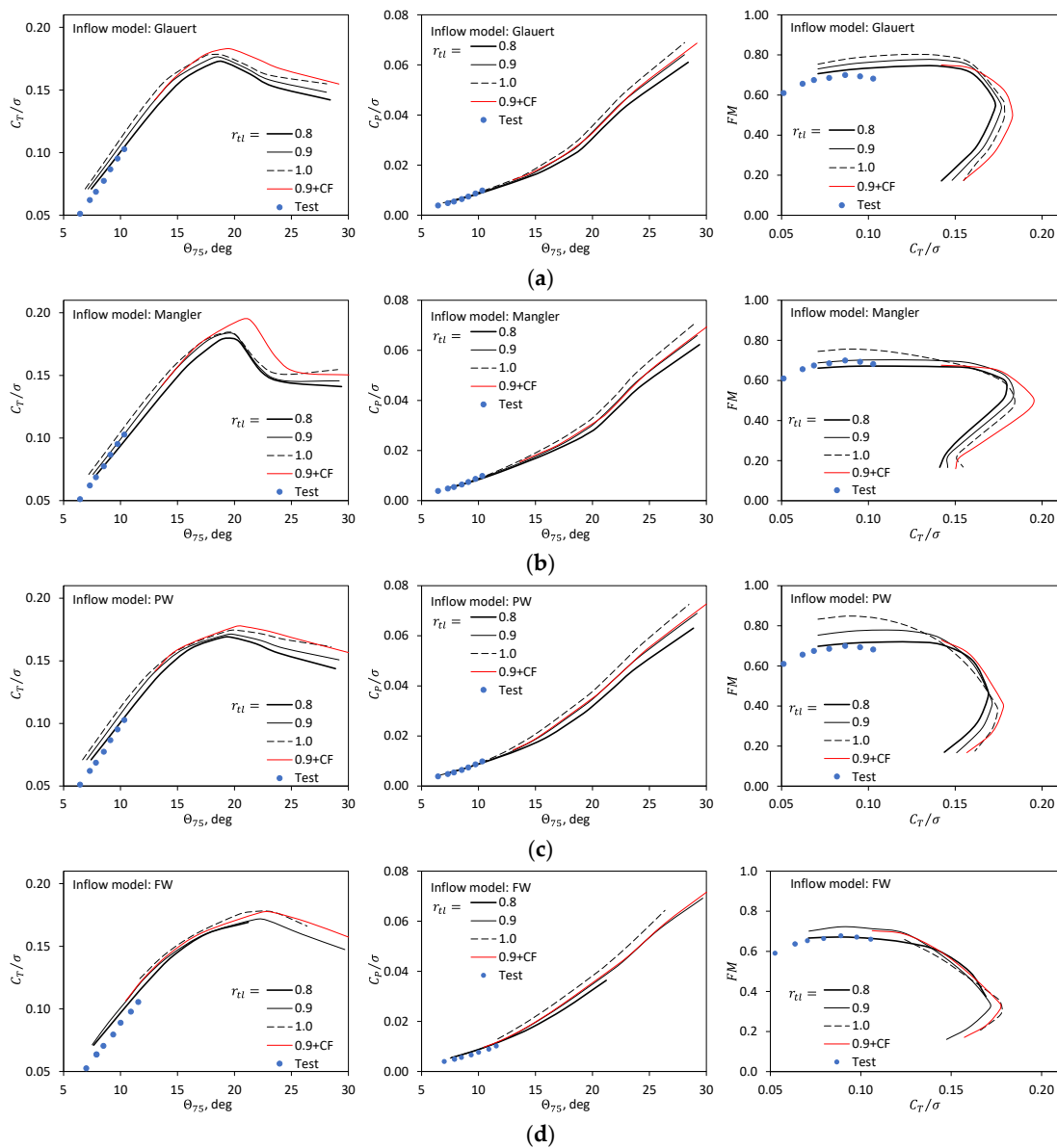


Figure 11. Influence of the inflow model, the tip loss parameter r_{tl} , and curvature flow CF model on thrust (left), power (middle), and figure of merit (right). (a) Constant inflow (Glauert); (b) Nonlinear inflow (Mangler); (c) Prescribed wake (PW); (d) Free-wake (FW).

The blue dots are experimental data from the Bo105 model scale rotor obtained in the DNW [46] that reach up to only $C_T/\sigma = 0.106$ and remain within the attached flow regime. In contrast to the assumptions made for the computations of this paper, the tested rotor blades were flexible, slightly dissimilar, and developed an increasing amount of steady elastic twist with rising thrust. The test was conducted in the open-jet closed test hall of the DNW-LLF. Therefore, air turbulence increased that was re-ingested into the rotor at high thrust, which caused increasing vibration, and a further thrust increase was abandoned.

The Glauert and prescribed wake (PW) inflow lead to similar results, with a gradual decrease in thrust in the post-stall regime. The Mangler model reaches the greatest maximum thrust of all models, with a larger loss of thrust in the post-stall area. In all cases, no tip loss $r_{tl} = 1.0$ allows for the highest maximum thrust. With r_{tl} moving inboard, maximum thrust is reduced continuously because of lift loss mainly at the blade tip, and to a much lesser degree also at the blade root.

Regarding the power prediction, all inflow model results appear rather similar to each other. The experimental thrust and power curves are matched by all inflow methods, with the best fit achieved by the Mangler model. The effect of r_{tl} variation is in accordance with its impact on thrust. Any loss of lift at the blade tip is associated with a reduction mainly in the induced drag and also of the airfoil drag there, and due to the long moment arm to the rotor center, this reduces the power.

The figure of merit FM is very sensitive to power prediction. The best fit to the test data is seen for the Mangler model with a tip loss beginning between $r_{tl} = 0.8$ and 0.9 . As expected, the highest possible FM is obtained without tip loss, $r_{tl} = 1.0$, and in the region around $C_T/\sigma = 0.11$, i.e., in the region of attached flow, but close to stall.

The curvature flow model (CF) was only applied to the $r_{tl} = 0.9$ setting and its results are given by the red lines. As long as the flow is attached, there appears to be no difference from the cases without the inclusion of the CF model. Once stall starts to develop, the CF model generates a delay in the steady stall angle of attack especially in the inboard region of the rotor blade with an increase in the maximum lift coefficient to larger values; see Figure 5. This leads to a higher maximum thrust capability of the rotor, and also a higher thrust in the post-stall regime, while the power appears only slightly increased over the value without the CF model.

The same is seen in the impact of the CF model on the FM , independent of the inflow model used. In attached flow, the slight increase in power results in a slightly lower FM than without the CF model. Although the CF model allows for a higher maximum thrust, the FM at the highest possible thrust is similar to that without the CF model employed.

The results for the individual maximum rotor thrust achievable with the various inflow models are summarized in Figure 12a. For each of the inflow models used, the increase in r_{tl} from 0.8 to 1 increases the maximum trimmable thrust by about the same amount, and the same applies when adding the CF model. The respective power required for the maximum thrust is shown in Figure 12b. The power increases according to the thrust of the individual inflow model shown in Figure 12a, and only the PW model results in a steeper increase in power than the other inflow models.

The power sensitivity with respect to the tip loss region cannot directly be judged by Figure 12b, because at $r_{tl} = 0.8$, a significantly smaller maximum thrust is obtained than for a value of 1 . For $r_{tl} = 0.8$, less power is expected at the blade tip because of lower induced and airfoil drag due to the smaller angles of attack. But any loss of lift at the tip must be compensated for by more inboard lift and hence more induced and airfoil drag there, until the maximum rotor thrust is reached.

The CF model increases the power required at maximum thrust in all cases, in agreement with the increase in the maximum thrust itself. It is also observed in Figure 12 that the power level depends on the inflow model used. Although the PW and FW inflow models reach the lowest maximum thrust, their power is the highest. The Mangler inflow model predicts higher thrust, but also requires more power than the Glauert inflow. FW is close to PW in maximum thrust capability, but the power required is always higher. The reason for

these results requires the analysis of the radial distribution of aerodynamic parameters, as given in the next section.

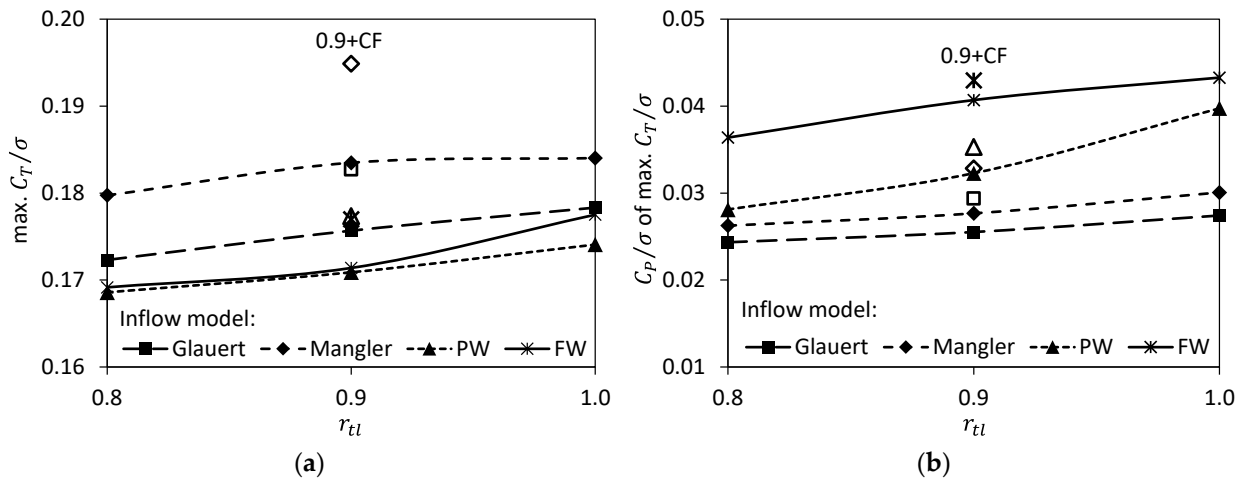


Figure 12. Influence of tip loss, inflow, and CF models on maximum rotor thrust and power required. (a) maximum trimmable thrust; (b) power required at maximum trimmable thrust.

3.3. Distribution of Aerodynamic Parameters

In order to understand the development of power in Figure 12b, first the radial distribution of the inflow ratio λ_i needs to be investigated. In Figure 13a, it is given for the nominal thrust ($C_T/\sigma = 0.071$, black curves), a rather high thrust commonly achieved by all inflow models ($C_T/\sigma = 0.16$, red curves), and under a condition of 5 deg in collective control angle larger than that of the individual maximum thrust. The latter is different for each inflow model (C_T/σ differs, blue curves), but in every case represents a deep stall condition for the rotor. The tip loss factor is set to $r_{tl} = 0.9$ in every case, and the different inflow models used are identified by different line styles.

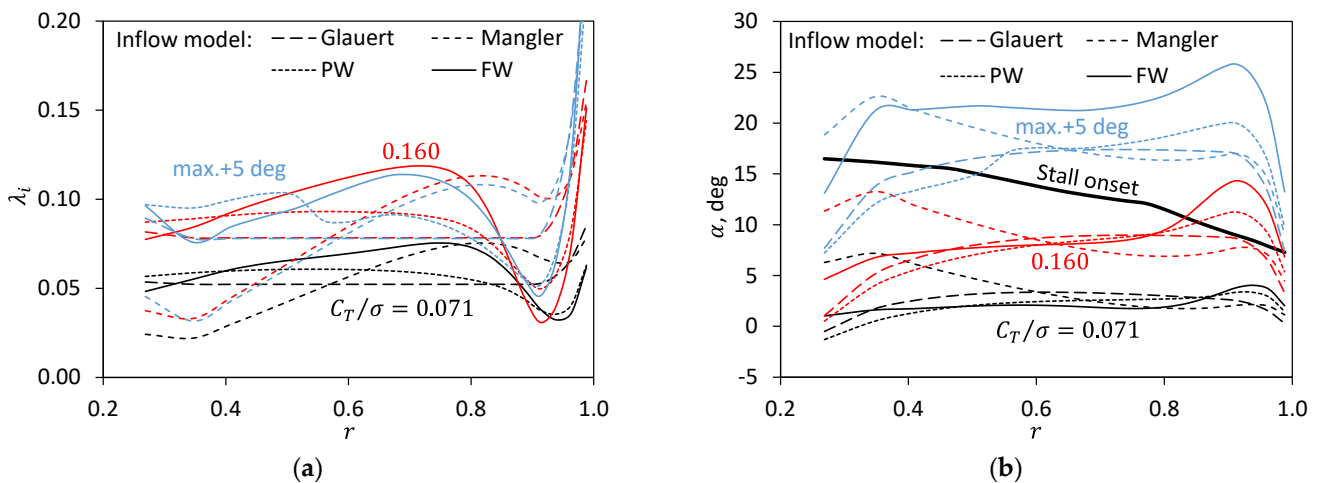


Figure 13. Radial distributions of aerodynamic parameters for various thrust levels and inflow models in hover, $r_{tl} = 0.9$. (a) inflow ratio; (b) section angle of attack.

Because of the tip loss beginning at $r_{tl} = 0.9$, the induced inflow progressively increases towards the tip and the root of the blade for all inflow models; compare this to $r_{tl} = 1.0$ (=2D from root to tip), as shown in Figure 9. Outboard of $r \approx 0.8$, the Mangler model generates the highest induced inflow and the PW and FW models the lowest, which is due to the tip vortex quickly moving inboard and then inducing an upwash at the outer region $0.85 < r < 1$. Inboard of $r \approx 0.6$, the PW and FW generate the highest inflow due to their wake contraction, and the Mangler model the lowest.

The section angle of attack α can be computed based on the blade pretwist, the collective control angle required for the respective thrust, the circumferential velocity, and the inflow. This is shown in Figure 13b for the same conditions as in Figure 13a, together with the steady stall onset boundary (see Figure 4). At the inner radial stations with small circumferential velocities, the same inflow ratio leads to larger angles of attack than at the outer radial stations with large circumferential velocities.

At the tip region, the PW and FW models show the smallest inflow and therefore the largest angle of attack, the inverse of which is true at the regions inboard of $r \approx 0.6$. For the thrust level of $C_T/\sigma = 0.16$, the PW and FW models are the only ones that exceed the stall angle of attack near the tip region, while the Glauert and Mangler models remain below it. This is caused by the upwash in the tip region due to the wake contraction in the PW and FW inflow models. This upwash generates more lift and drag, and because of the large distance to the hub center, more is power required here than the other inflow models.

By increasing the collective control by 5 deg above the maximum trimmable thrust (blue lines), the majority of radial stations are under post-stall conditions at very high angles of attack. Only the Glauert and PW inflow models are below the stall inboard of $r \approx 0.45$, owing to the higher inflow ratio when compared to the Mangler model. The overall inflow is slightly lower than for $C_T/\sigma = 0.16$, because the rotor thrust under this deep stall condition is less.

In Figure 14a,b, the respective distributions of the section normal force, C_n , and moment coefficient about the quarter chord, C_m , are plotted. The generally small angles of attack for $C_T/\sigma = 0.071$ are within the attached flow regime far away from stall all over the blade, as was given in Figure 13b. This leads to moderate normal force and small negative moment coefficients (because of airfoil camber).

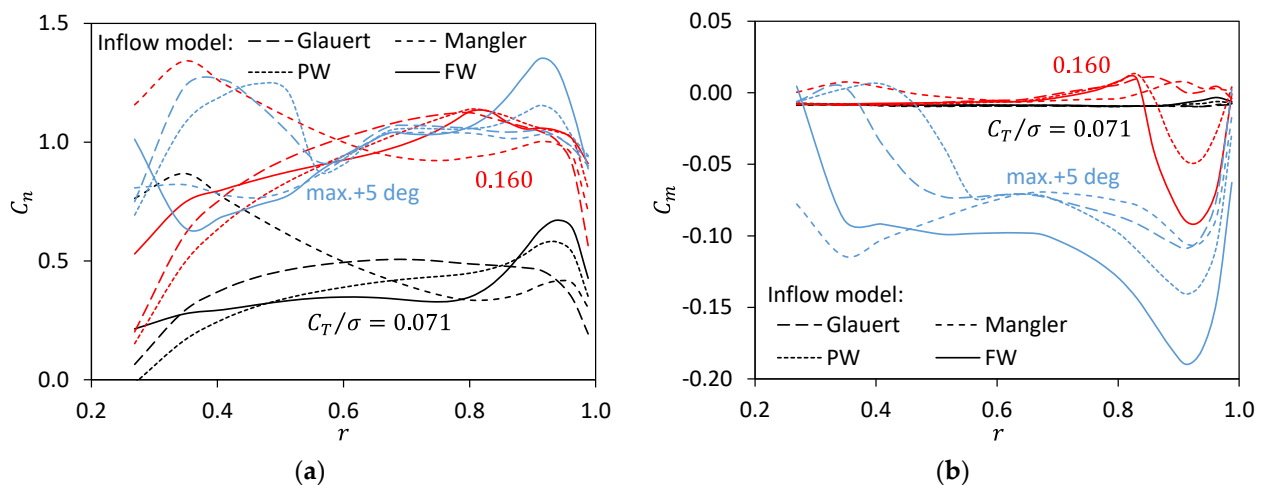


Figure 14. Radial distributions of aerodynamic coefficients for various thrust levels and inflow models in hover, $r_{H1} = 0.9$. (a) normal force coefficient; (b) moment coefficient.

The high thrust of $C_T/\sigma = 0.160$ comes along with higher normal force coefficients. Figure 13b indicates the stall for the PW and FW models in the outer region $0.85 < r < 1$. This cannot immediately be seen in the normal force coefficient in Figure 14a, because the stall behavior at this Mach number is very gradual; see Figure 5b. However, the stall is seen in the moment coefficient of the PW and FW models with the corresponding red curves dropping sharply to larger negative values near the tip; see Figure 14b. The other blade areas are close to stall, indicated by zero or slightly positive moment coefficients.

The blue lines are for the case where the collective control angle is increased by 5 deg over that of the individual maximum thrust achieved by the different inflow models. Nearly all radial stations are under a deep stall condition as indicated by Figure 13b. Although the normal force coefficients are at the same levels (in the stalled region) as for

the $C_T/\sigma = 0.160$ case, the moment coefficients indicate deep stall almost all over the blade by their large negative values.

This is because from $r \approx 0.65$ to the tip, the Mach numbers exceed 0.4, and the stall characteristics of the normal force coefficient flatten out; see Figure 5b. For $r < 0.6$, however, the FW and Mangler inflow models show a significant loss of normal force coefficient in Figure 14a, while the Glauert and PW inflow models remain below stall, which results in large C_n . In this area, the moment coefficients for these two inflow models are close to zero, which indicates angles of attack close to, but not beyond, stall (Figure 14b).

3.4. The Maximum Trimmable Thrust

As shown in Figures 11 and 12a, the maximum trimmable thrust varies depending on the inflow model, the tip loss model, and the CF model. In the following, $r_{tl} = 0.9$ is used. Radial distributions of the inflow, angle of attack including stall onset, normal force, and moment coefficients at the individual maximum trimmable thrust are shown. As before, the inflow models are identified by the line styles, and black curves are without the CF model, while the curves including it are red. In general, the inclusion of the CF model allows for a higher maximum thrust for all inflow models; see Figure 12a.

The inflow distributions are shown in Figure 15a and are rather comparable to the curves for $C_T/\sigma = 0.160$ in Figure 13, but at a higher value due to a higher thrust. Recall that each of the curves is for a different thrust; therefore, the mean of the inflow models differs as well. Due to the higher thrust with the CF model involved, the red curves are slightly higher than the black ones.

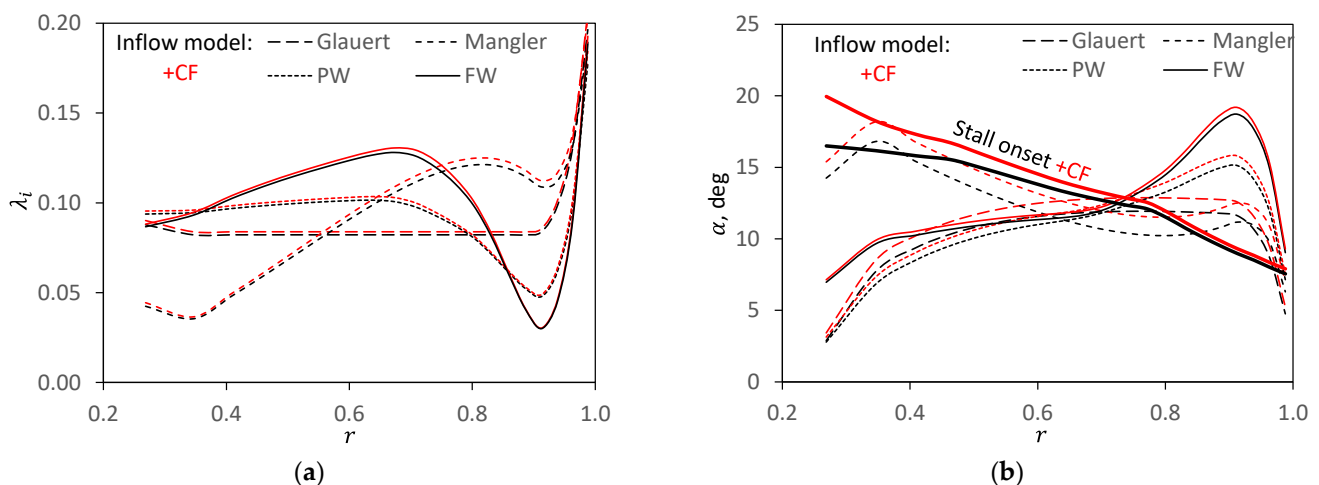


Figure 15. Radial distributions of aerodynamic parameters for maximum trimmable thrust and different inflow models in hover, $r_{tl} = 0.9$. (a) inflow ratio; (b) section angle of attack.

The distribution of angles of attack along the span is given in Figure 15b, which can be compared with the curves for $C_T/\sigma = 0.160$ of Figure 13b, but here for the higher maximum trimmable thrust. Independent of the CF model, all inflow models exceed the stall angle near the tip region. Most prominent are here the PW and FW models, which are the only ones that include the tip vortex upwash due to the wake contraction, and thus increase the angle of attack there. In the region $0.75 < r < 0.95$, the angle of attack exceeds the stall angle. Inboard of it, the Glauert, PW, and FW models generate angles of attack which are significantly lower than the Mangler model. Therefore, with the Mangler model at $r \approx 0.35$, the stall angle is slightly exceeded.

The normal force and moment coefficient distributions for the maximum trimmable thrust show the stall effects of normal force and moment coefficients in Figure 16, which can be compared to Figure 14 for the lower thrust of $C_T/\sigma = 0.160$. Because the Mangler inflow model leads to angles of attack rather close to stall all over the radius (see Figure 15b), its

distribution of C_n values is close to the maximum normal force coefficient at each of the radial positions and its respective Mach number.

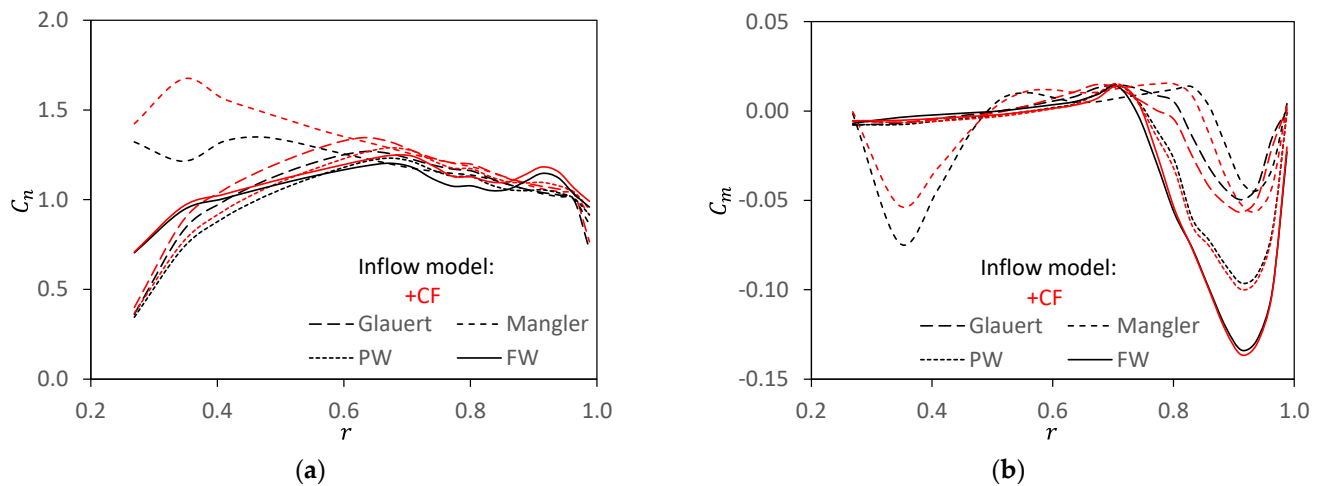


Figure 16. Radial distributions of aerodynamic coefficients for maximum trimmable thrust and inflow models in hover, $r_{tl} = 0.9$. (a) normal force coefficient; (b) moment coefficient.

In the region near the tip for $r > 0.75$, all inflow models generate rather similar C_n values, despite very different angles of attack. This is due to the flat $C_n(\alpha)$ curves in the post-stall regime at the higher subsonic Mach numbers experienced there; see Figure 5b.

Near $r \approx 0.35$, the Mangler model leads to slight stall without the CF model (black curve; see Figure 15b). Due to the small Mach number there (see Figure 5a), the post-stall region is accompanied by a moderate drop in normal force coefficient, which is seen at that position in Figure 16a. When including the CF model, the angle of attack here just reaches the stall angle, and the normal force coefficient reaches its highest value.

Finally, the moment coefficients for these conditions of maximum trimmable thrust are shown in Figure 16b. The moment coefficient is much more sensitive to stall than the normal force coefficient, because in attached flow it remains at small negative values, but during stall, sharply drops to larger negative values. This is seen especially at the tip region for all inflow models, and also near the root of the blade for the Mangler inflow model.

Concluding the hover investigations, the maximum trimmable thrust of the rotor always includes stall over some radial extent of the blade, at least for this rotor blade geometry. Therefore, to further enhance the thrust capability, the blade design must be changed in terms of twist distribution, chord distribution, and airfoil selection, but that is outside of the scope of this paper. The range of C_T/σ obtained with all the various combinations of inflow model, realistic r_{tl} values of 0.8 and 0.9, and the CF model switched on or off, covers values from 0.168 to 0.184 with one exception obtained using the Mangler inflow model plus CF reaching 0.196, as given in Figure 12a and also included in Figure 1 for comparison with existing test data and estimates. For the highest thrusts, results with $r_{tl} = 0.8$ are close to Johnson's estimate.

3.5. Effect of the Vortex Shedding (VS) Model

Adding the VS model impacts all blade sections operating in the stalled region, as shown in Figures 6 and 7 for steady, unsteady, and yawed airfoil coefficients. In the results obtained at maximum thrust with the Glauert model and $r_{tl} = 0.9$ tip loss formulation, airfoil stall is experienced near the blade tip; see Figure 15b. The time history of the normal force coefficient C_n at a radial position of $r = 0.913$ is shown in Figure 17a for one rotor revolution, and the rotor thrust C_T/σ is given in Figure 17b. The results without the VS model and with it are compared with each other.

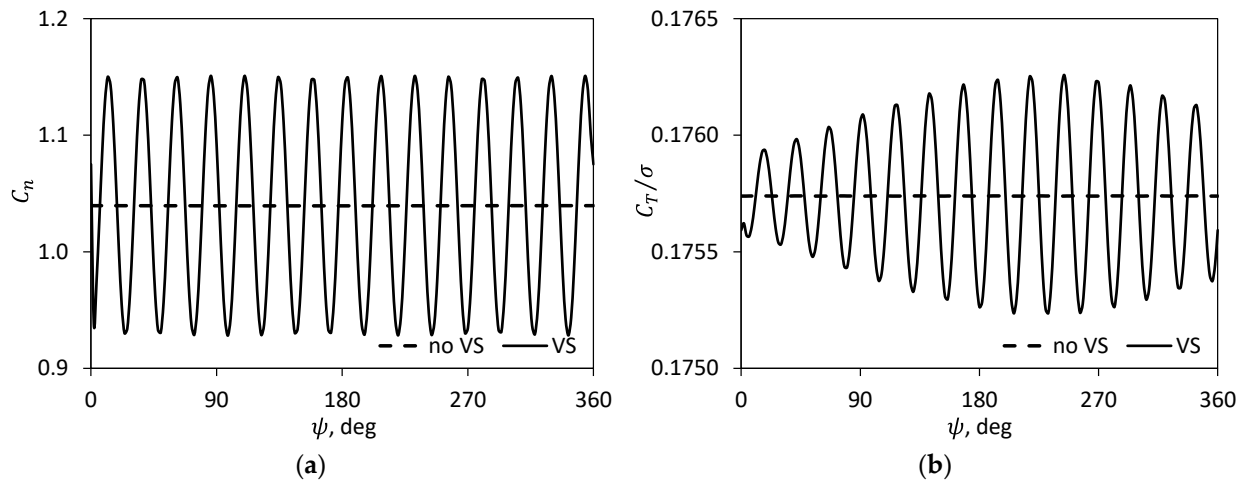


Figure 17. Effect of the VS model on aerodynamic coefficients at maximum thrust in hover, $r_{tl} = 0.9$, Glauert inflow. **(a)** normal force coefficient at $r = 0.913$; **(b)** thrust coefficient.

At this outboard region near the blade tip, a Mach number of ca. 0.58 is present and the frequency of fluctuations is near the 15th harmonic at the blade, with a magnitude of about $\Delta C_n = 0.11$. The frequency of C_n oscillations is a function of the Mach number and varies between the radial stations of the blade. However, the mean value is that of the steady stall C_n of the result without the VS model. The summation of all four blades results in the rotor thrust as shown in Figure 17b. Again, the steady computation without the VS model represents the mean value of the result including the VS model. Due to the summation of thrust from all four blades, the remaining frequency content has changed. However, it is seen that some non-harmonic fluctuations in thrust remain. This necessitates the adaptation of the trim strategy, i.e., allowing for some bandwidth of thrust to develop, or applying a long-term averaging of the results, instead of a single revolution.

3.6. Effect of Unsteady Aerodynamic Modeling

It must first be recalled that in this study, the blades are modeled as rigid bodies without elasticity to focus solely on the aerodynamic effects. After all aerodynamic transients during the trim process have died out, the hovering condition always results in a steady aerodynamic environment at the blade elements for the global downwash models. Without any unsteadiness of the input, the results obtained with steady and unsteady aerodynamics models become identical. Using PW with tip (and possibly secondary) trailed vortices, or FW with trailed and shed vortex elements, any unsteadiness of the blade bound circulation (either generated due to the trim steps or by the VS model) will be fed into the wake system. Consequently, a time-varying blade circulation strength will result in a time-varying induced velocity distribution at the blade elements via the wake-induced velocities. However, in the current setup, the trailed and shed vortex circulations are low-pass filtered to the first six rotor harmonics to account for fundamental blade load variations, but not for such high-frequency content as shown in Figure 17a. In addition, a soft coupling strategy for both PW and FW is applied with updates of the wake geometry and its induced velocities only after a trim step has converged. Therefore, in the current setup, only a small amount of unsteadiness was developing, as exemplarily shown in Figure 17b. This will likely change in a tight coupling between rotor and wake at each time step of the simulation at the expense of significantly higher computational effort, but that is outside of the scope of this article.

4. Conclusions

In this article, the impact of inflow models (Glauert, Mangler, prescribed (PW) and free-wake (FW)), radial extent of tip loss (r_{tl}), stall delay due to curvature flow (CF), and post-stall vortex shedding (VS) on maximum rotor thrust in hover have been investigated. A

Bo105 model-scale rotor was used for the study with rigid blades to eliminate the influence of blade flexibility on the results. The results for global parameters (thrust/power curves, figure of merit (*FM*)) were investigated in detail via the analysis of the radial distributions of the inflow, blade section angle of attack, stall angle of attack, and airfoil normal force and moment coefficients. The following conclusions can be drawn:

Trim strategy and global observations:

- In attached flow, a trim to thrust converges quickly due to a large derivative $dC_T/d\Theta_{75}$.
- In the vicinity of maximum thrust, a trim to thrust is difficult, because $dC_T/d\Theta_{75}$ becomes zero at the maximum thrust. It even changes its sign for higher control angles. In contrast, a trim to power converges quickly there, because the derivative $dC_P/d\Theta_{75}$ grows progressively in this regime. However, to match a specific thrust, some iterations of power trim are needed.
- The maximum possible thrust is similar for the Glauert, PW, and FW inflow models, and highest for the Mangler inflow model.
- The maximum figure of merit (*FM*) is found in the range of $C_T/\sigma = 0.1$ to 0.12 , significantly below the maximum possible thrust of $C_T/\sigma \geq 0.17$. The larger the tip loss, the smaller the *FM*. Up to the maximum *FM*, the CF model has virtually no impact on the results, because max. *FM* is obtained under the attached flow conditions.

Impact of inflow models:

- Induced inflow ratio distributions vary significantly between the inflow models and accordingly vary the distributions of the resulting angle of attack. This has a significant impact on where the stall angle is reached first, because the local stall angle depends on the local Mach number.
- The Glauert model provides constant inflow over the entire radius. It leads to a rather constant angle of attack distribution. Therefore, stall is experienced first in the blade tip region where the stall angle is the lowest.
- The Mangler model generates the lowest inflow of all inflow models at the blade root, leading to large angles of attack there. This is advantageous because the stall angle at the low Mach numbers near the root are large as well. In the outer part of the blade, it generates the largest inflow of the models; hence, the smallest angles of attack and therefore blade tip stall are reduced significantly.
- The prescribed wake (PW) model's inflow distributions are rather constant inboard of $r \approx 0.8$ and a little larger than the Glauert inflow. Outboard the PW inflow is significantly lower due to the upwash generated by the contracted wake geometry. Therefore, angles of attack are slightly below those of the Glauert model inboard of $r \approx 0.8$ and slightly larger outboard.
- Free-wake (FW) inflow distributions which are near the Glauert at the blade root, reach the largest values of all inflow models at about $r \approx 0.7$, and the lowest values of all at $r \approx 0.85$. The resulting angles of attack are between the Glauert and the Mangler models near the blade root, close to the Glauert and PW models in the mid region of the blade, and highest at the blade tip for $r > 0.85$. Therefore, blade tip stall develops first for this model.
- The highest possible thrust is predicted by the Mangler model, because of its low inflow in the inboard region and high inflow in the outer region of the blade. The resulting angle of attack distribution fits best to the stall angle distribution.

Tip loss and CF modeling impact:

- The tip loss model progressively increases the induced velocities at both ends of the blade, such that zero lift results at the ends. This reduces the angle of attack from r_{tl} on, progressively towards the end, therefore alleviating stall near the blade tip and root.
- Increasing the tip loss region reduces the maximum possible thrust due to the increased loss of lift in the tip and root regions. Reasonable values for high thrust range from $r_{tl} = 0.8 - 0.9$.

- The curvature flow (CF) model increases the linear lift range by an increase in the steady stall angle from small values at the blade tip progressively to larger values at the blade root. This has a significant impact on increasing the maximum thrust prediction, because it allows for larger angles of attack. This is the reason why the Mangler model predicts the largest possible thrust of all inflow models.

Funding: This research is based on institutional funding of DLR.

Data Availability Statement: The data presented in this study are partly available on request from the author. The data are in parts not publicly available due to proprietary reasons.

Conflicts of Interest: The author declares no conflicts of interest.

References

1. Bailey, F.J., Jr.; Gustafson, F.B. *Observations in Flight of the Region of Stalled Flow over the Blades of an Autogiro Rotor*; NACA TN 741; NTRS: Washington, DC, USA, 1939.
2. Gustafson, F.B.; Myers, G.C., Jr. *Stalling of Helicopter Blades (Contributions to the Aerodynamics of Rotary-Wing Aircraft)*; NACA TR 840; NTRS: Washington, DC, USA, 1946; pp. 105–110.
3. Sissingh, G. Beitrag zur Aerodynamik der Drehflügelflugzeuge. Ph.D. Thesis, TH Hannover, Hanover, Germany, 1940.
4. Focke, H. Fortschritte des Hubschraubers. Schriften der Deutschen Akademie der Luftfahrtforschung, No. 1070/43g, 1943.
5. van der Wall, B.G. (Ed.) *Göttinger Monograph N: German Research and Development on Rotary-Wing Aircraft, (1939 to 1945)*; AIAA Library of Flight: Reston, VA, USA, 2015. [CrossRef]
6. Bellinger, E.D. Analytical Investigation of the Effects of Blade Flexibility, Unsteady Aerodynamics, and Variable Inflow on Helicopter Rotor Stall Characteristics. *J. Am. Helicopter Soc.* **1972**, *17*, 35–44. [CrossRef]
7. Hardy, W.G.S. Effects of Reynolds Number on Rotor Stall. In Proceedings of the Symposium on Status of Testing and Modeling Techniques for V/STOL Aircraft, Philadelphia, PA, USA, 26–28 October 1972.
8. McCroskey, W.J.; Fisher, R.K., Jr. Detailed Aerodynamic Measurements on a Model Rotor in the Blade Stall Regime. *J. Am. Helicopter Soc.* **1972**, *17*, 20–30. [CrossRef]
9. Landgrebe, A.J.; Bellinger, E.D. A Systematic Study of Helicopter Rotor Stall using Model Rotors. In Proceedings of the 30th Annual Forum of the American Helicopter Society, Washington, DC, USA, 7–9 May 1974.
10. Amer, K.B.; LaForge, S.V. Maximum Rotor Thrust Capabilities, Articulated and Teetering Rotors. *J. Am. Helicopter Soc.* **1977**, *22*, 11–12. [CrossRef]
11. McHugh, F.J. What are the Lift and Propulsive Force Limits at High Speed for the Conventional Rotor? In Proceedings of the 34th Annual National Forum of the American Helicopter Society, Washington, DC, USA, 15–17 May 1978.
12. Yeo, H. Calculation of Rotor Performance and Loads Under Stalled Conditions. In Proceedings of the 59th Annual Forum and Technology Display, Phoenix, AZ, USA, 6–8 May 2003.
13. Johnson, W. Technology Drivers in the Development of CAMRAD II. In Proceedings of the American Helicopter Society Aeromechanics Specialist Meeting, San Francisco, CA, USA, 19–21 January 1994.
14. Johnson, W. *Rotorcraft Aeromechanics*; Cambridge University Press: New York, NY, USA, 2013; Chapter 12, p. 456. [CrossRef]
15. Petot, D.; Arnaud, G.; Harrison, R.; Stevens, J.; Dieterich, O.; van der Wall, B.G.; Young, C.; Széchenyi, E. Stall Effects and Blade Torsion—An Evaluation of Predictive Tools. *J. Am. Helicopter Soc.* **1999**, *44*, 320–332. [CrossRef]
16. AIAA Rotorcraft Hover Prediction Workshop. Available online: <https://www.aiaa-hpw.org> (accessed on 8 April 2024).
17. Norman, T.R.; Heineck, J.T.; Schairer, E.T.; Schaeffer, N.W.; Wagner, L.N.; Yamauchi, G.K.; Overmeyer, A.D.; Ramasamy, M.; Cameron, C.G.; Dominguez, M.; et al. Fundamental Test of a Hovering Rotor: Comprehensive Measurements for CFD Validation. In Proceedings of the VFS 79th Annual Forum & Technology Display, West Palm Beach, FL, USA, 16–18 May 2023.
18. Zagaglia, D.; Croke, A.D.; Green, R.B.; Barakos, G.N. Development of the UK National Rotor Rig for Aeroelastic Testing of Rotary Wings. In Proceedings of the 49th European Rotorcraft Forum, Bückeburg, Germany, 5–7 September 2023.
19. Whitehouse, G.R.; Wachspress, D.A.; Quackenbush, T.R. Predicting the Influence of Blade Shape on Hover Performance with Comprehensive Analyses. *AIAA J. Aircr.* **2018**, *55*, 111–121. [CrossRef]
20. Whitehouse, G.R.; Wachspress, D.A.; Quackenbush, T.R. Correction: Predicting Hovering Rotor Performance with Comprehensive Analyses, Revisited. In Proceedings of the AIAA SciTech Forum, San Diego, CA, USA, 3–7 January 2022. [CrossRef]
21. Betz, A. Schraubenpropeller mit geringstem Energieverlust (Propeller with Minimum Energy Loss). With an addendum from L. Prandtl, Göttinger Nachrichten 1919; p. 193.
22. van der Wall, B.G. Factors Affecting Rotor Stall Computation by Comprehensive Rotor Codes. In Proceedings of the 49th European Rotorcraft Forum, Bückeburg, Germany, 5–7 September 2023.
23. van der Wall, B.G.; Lim, J.W.; Smith, M.; Jung, S.N.; Bailly, J.; Baeder, J.D.; Boyd, D.D. The HART II International Workshop: An Assessment of the State-of-the-Art in Comprehensive Code Prediction. *CEAS Aeronaut. J.* **2013**, *4*, 223–252. [CrossRef]
24. Gormont, R.E. *A Mathematical Model of Unsteady Aerodynamics and Radial Flow for Application to Helicopter Rotors*; USAAVLABS TR 72-67; U.S. Army Air Mobility Research and Development Laboratory: Fort Eustis, VA, USA, 1973.

25. Bielawa, R.L. Synthesized Airfoil Data Method with Applications to Stall Flutter Calculations. In Proceedings of the 31st Annual Forum of the American Helicopter Society, Washington, DC, USA, 13–15 May 1975.
26. Tran, C.T.; Petot, D. A Semi-Empirical Model for the Dynamic Stall of Airfoils in View of the Application to the Calculation of Responses of Helicopter Blade in Forward Flight. *Vertica* **1981**, *5*, 35–53.
27. Beddoes, T.S. Practical Computation of Unsteady Lift. *Vertica* **1983**, *7*, 183–197.
28. Gangwani, S.T. Synthesized Airfoil Data Method for Prediction of Dynamic Stall and Unsteady Airloads. *Vertica* **1984**, *8*, 93–118.
29. Leiss, U. A Consistent Mathematical Model to Simulate Steady and Unsteady Rotor-Blade Aerodynamics. In Proceedings of the 10th European Rotorcraft Forum, The Hague, The Netherlands, 28–31 August 1984.
30. Leiss, U. Unsteady Sweep—A Key to Simulation of Three-Dimensional Rotor Blade Airloads. In Proceedings of the 11th European Rotorcraft Forum, London, UK, 10–13 September 1985.
31. Leishman, J.G.; Beddoes, T.S. A Semi-Empirical Model for Dynamic Stall. *J. Am. Helicopter Soc.* **1989**, *34*, 3–17. [[CrossRef](#)]
32. Petot, D. Differential Equation Modeling of Dynamic Stall. In *La Recherche Aérospatiale*; Corrections Dated October 1990; ONERA: Chatillon-sous-Bagneuse, France, 1989; Volume 5, pp. 59–72.
33. Truong, V.K. A 2-D Dynamic Stall Model Based on a Hopf Bifurcation. In Proceedings of the 19th European Rotorcraft Forum, Marseilles, France, 14–16 September 1998.
34. van der Wall, B.G. An Analytical Model of Unsteady Profile Aerodynamics and its Application to a Rotor Simulation Program. In Proceedings of the 15th European Rotorcraft Forum, Amsterdam, The Netherlands, 12–15 September 1989.
35. Viterna, L.A.; Corrigan, R.D. *Fixed Pitch Rotor Performance of Large Horizontal Axis Wind Turbines*; NASA-CP-2230; NTRS: Washington, DC, USA, 1981; pp. 69–86.
36. Theodorsen, T. *General Theory of Aerodynamic Instability and the Mechanism of Flutter*; NACA Report 496; NTRS: Washington, DC, USA, 1935.
37. Glauert, H. *A General Theory of the Autogyro*; ARC R&M 1111; Her Majesties Stationary Office (HMSO): London, UK, 1926.
38. Meijer-Drees, J.M. A Theory of Airflow Through Rotors and its Application to Some Helicopter Problems. *J. Helicopter Assoc. Great Br.* **1949**, *3*, 79–104. [[CrossRef](#)]
39. Mangler, K.W.; Squire, H.B. *The Induced Velocity Field of a Rotor*; ARC R&M 2642; Her Majesties Stationary Office (HMSO): London, UK, 1950.
40. van der Wall, B.G.; Roth, M. Free-Wake Analysis on Massively Parallel Computers and Validation with HART Test Data. In Proceedings of the 53rd Annual Forum of the American Helicopter Society, Virginia Beach, VA, USA, 29 April–1 May 1997.
41. Beddoes, T.S. A Wake Model for High Resolution Airloads. In Proceedings of the International Conference on Rotorcraft Basic Research, National Institute of Environmental Health Sciences Research, Triangle Park, NC, USA, 19–21 February 1985.
42. van der Wall, B.G. The Effect of HHC on the Vortex Convection in the Wake of a Helicopter Rotor. *Aerosp. Sci. Technol.* **2000**, *4*, 320–336. [[CrossRef](#)]
43. van der Wall, B.G.; Yin, J. Semi-Empirical Modeling of Fuselage-Rotor Interference for Comprehensive Codes: Influence of Angle of Attack. *CEAS Aeronaut. J.* **2015**, *6*, 557–574. [[CrossRef](#)]
44. Wheatley, J.B. *An Aerodynamic Analysis of the Autogyro Rotor with a Comparison between Calculated and Experimental Results*; NACA TR 487; NTRS: Washington, DC, USA, 1934.
45. Sissingh, G.J. Beitrag zur Aerodynamik der Drehflügelflugzeuge. *Luftfahrt-Forsch.* **1938**, *15*, 290–302, Translation in: *Contributions to the Aerodynamics of Rotary-Wing Aircraft*; NACA TM 921, 1939.
46. Küfmann, P.M.; Bartels, R.; van der Wall, B.G.; Schneider, O.; Holthusen, H.; Postma, J. The Second Wind-Tunnel Test of DLR's Multiple Swashplate System-IBC on a five-bladed rotor with fuselage-mounted (fixed frame) actuators. *CEAS Aeronaut. J.* **2019**, *10*, 385–402. [[CrossRef](#)]

Disclaimer/Publisher's Note: The statements, opinions and data contained in all publications are solely those of the individual author(s) and contributor(s) and not of MDPI and/or the editor(s). MDPI and/or the editor(s) disclaim responsibility for any injury to people or property resulting from any ideas, methods, instructions or products referred to in the content.